PCCP

Accepted Manuscript

This article can be cited before page numbers have been issued, to do this please use: G. Gibson, Z. Wang, C. Hardacre and W. Lin, *Phys. Chem. Chem. Phys.*, 2017, DOI: 10.1039/C6CP06906A.

View Article Online
DOI: 10.1039/C6CP06906A

Journal Name

ARTICLE

Insights into the Mechanism of Electrochemical Ozone Production via Water Splitting on the Ni and Sb Doped SnO_2 Catalyst

Received 00th January 20xx,
Accepted 00th January 20xx

DOI: 10.1039/x0xx00000x

www.rsc.org/

Gregory Gibson,[a,c] Ziyun Wang[b], Christopher Hardacre[b] and Wen-Feng Lin*[a]

The H_2O splitting mechanism is a very attractive alternative used in electrochemistry for the formation of O_3. The most efficient catalysts employed for this reaction at room temperature are SnO_2-based, in particular the Ni/Sb-SnO_2 catalyst. In order to investigate the H_2O splitting mechanism Density Functional Theory (DFT) was performed on a Ni/Sb-SnO_2 surface with oxygen vacancies. By calculating different SnO_2 facets, the (110) facet was deemed most stable, and further doped with Sb and Ni. On this surface, the H_2O splitting mechanism was modelled paying particular attention to the final two steps, the formation of O_2 and O_3. Previous studies on β-PbO_2 have shown that the final step in the reaction (the formation of O_3) occurs via an Eley-Rideal style interaction where surface O_2 desorbs before attacking surface O to form O_3. It is revealed that for Ni/Sb-SnO_2, although the overall reaction is the same the surface mechanism is different. The formation of O_3 is found to occur through a Langmuir-Hinshelwood mechanism as opposed to Eley-Rideal. In addition to this the relevant adsorption energies (E_{ads}), Gibb's free energy (ΔG_{rxn}) and activation barriers (E_{act}) for the final two steps modelled in the gas phase have been shown; providing the basis for a tool to develop new materials with higher current efficiencies.

Introduction

In the last few decades, the treatment of wastewater via Advanced Oxidation Processes (AOP's) using ozone (O_3) as the principal oxidant has been investigated.[1-5] O_3 is a strong oxidant, the second strongest after chlorine, with an oxidation potential of 2.07 V. For this reason, it is a viable option as a replacement for chlorine as a water disinfectant. When using O_3 as a disinfectant, the main advantage over chlorine is that few harmful by-products are produced whereas chlorine produces halogenated complexes on reaction. The applications of O_3 are not limited to water treatment as more recent studies outline its application in healthcare[6, 7], sterilization[8, 9] and chemical synthesis[10]. The traditional method of generating O_3 is via a Cold Corona Discharge Reactor which occurs via the following reaction:

$$\frac{3}{2}O_2 \rightarrow O_3 \qquad \Delta H^0_{298} = 34.1\ kcal\ mol^{-1} \qquad \text{(R1)}$$

In this process, O_2 passes through the reactor, where the O_2 molecules dissociate to O atoms before interacting with further O_2 to form O_3. Although a simple method, the O_3 is formed in the gas phase making it difficult for aqueous applications. The current efficiency (CE) tends to be low with values reported of between 2-7 %[11, 12] depending on the source of O_2.

A more promising method is to produce O_3 via the electrochemical process of water splitting known as Electrochemical Ozone Production (EOP). This is not a new process with previous work being carried out on various different anodes such as Pt[13, 14], β-PbO_2[15-17], BDD[18, 19] and Ni/Sb-SnO_2[20-22] anode materials. The electrochemical splitting of water can occur through either a 4 or 6 step electron process shown in Reactions 2 and 3:

$$2H_2O \rightarrow O_2 + 4H^+ + 4e^- \qquad E^0 = 1.23\ V \qquad \text{(R2)}$$
$$3H_2O \rightarrow O_3 + 6H^+ + 6e^- \qquad E^0 = 1.51\ V \qquad \text{(R3)}$$

Reactions (2) and (3) show the same H_2O splitting mechanism with different products. The formation of O_2 can be deemed thermodynamically favoured in comparison to O_3 as can be seen from the E^0 values. Therein lays the major challenge with O_3 production. One way of overcoming the thermodynamics is to develop a system which requires a large overpotential for O_2 formation. This, in turn, will result in a surface with partially inhibited sites for O_2 formation and thus O_3 formation will be promoted. Of the many systems tested, Ni/Sb-SnO_2 reports the best CE values with O_3 yields reported at between 30 % to upwards of 50 % under ambient conditions[20-22].

The H_2O mechanism, although postulated by various groups, is still not well understood. Based on previous studies on β-PbO_2[23], the motivation of this research was to understand how the mechanism for the formation of O_3 proceeds on different catalysts using Density Functional Theory (DFT) calculations.

[a] Department of Chemical Engineering, Loughborough University, Loughborough, Leicestershire, LE11 3TU, UK. Email: w.lin@lboro.ac.uk
[b] School of Chemical Engineering and Analytical Science, The University of Manchester, Manchester, UK, M13 9PL
[c] School of Chemistry and Chemical Engineering, Queen's University of Belfast, Belfast, BT9 5AG, UK

For Ni/Sb-SnO_2, there are two mechanisms postulated based on either an O_3H intermediate or via direct O_3 formation. In this study the direct O_3 pathway is investigated. The Ni/Sb-SnO_2 catalyst is not one that has been studied using theoretical approaches before and thus little is known as to its preferred surface geometry. However, studies carried out by Batzill *et al.*[24] on investigating SnO_2 showed that the (110) facet was the most stable and so was used as the initial starting geometry. After further doping with Sb and Ni, the level of surface oxidation was tested and the direct O_3 mechanism examined.

Theoretical Methods

Density Functional Theory (DFT)

All DFT calculations were carried out with a periodic slab model using the Vienna Ab-initio simulation programme (VASP)[25-27]. A combination of the Generalised Gradient Approximation (GGA) and Perdew-Burke-Ernzernof (PBE) exchange correlation functional was applied[28]. The Projector Augmented Wave (PAW) method[29, 30] was utilized to describe the electron-ion interactions, and the plane wave basis expansion cut-off was set to 500 eV. All adsorption energies were optimised using the force-based conjugate gradient algorithm, whereas the transition states (TS) where located using the constrained minimization technique[31-33].

For the modelling of the Ni/Sb-SnO_2 surface, a stable SnO_2 facet must be generated before doping with Sb and Ni. The most stable SnO_2 surface facet was a (110) surface (Figure 1a)[24]. This was modelled as a (2 x 2) unit cell (6.37 Å x 6.70 Å) with a surface coverage of between 0.25 and 1 ML. The two-dimensional Brillouin integrations for each surface were sampled using *k*-points. The surfaces with a (2 x 2) unit cell were sampled using a 3 x 3 x 1 Monkhorst-Pack grid [34]. Ni/Sb-SnO_2 was modelled using a periodic 4-layer model with the lower two layers fixed and the upper two layers relaxed. Slab separation was provided normal to the surface by use of a 15 Å vacuum region.

To dope the surface with Sb and Ni a simple yet robust approach was applied. An Sb atom has replaced each of the four surface Sn atoms simultaneously to determine on which site it is most stable. Again geometry optimization is carried out with the lower two layers fixed and the upper two layers relaxed (Figure 1b).

To further dope the surface with Ni, the same approach for Sb was repeated. Each of the remaining Sn atoms is replaced with a Ni atom to determine the most stable arrangement across the top surface layer. Geometry optimization calculations are run again with the lower two layers fixed and upper two layers relaxed. Throughout each of these steps the slab separation will remain 15 Å. The Ni/Sb-SnO_2 catalyst was similar to the bulk SnO_2 (110) and thus the unit cell size was (2 x 2) with the *k*-point sampling being 3 x 3 x 1 (Figure 1c). All calculations for SnO_2, Sb-SnO_2 and Ni/Sb-SnO_2 were performed as spin-open.

In addition, the presence of surface defects or vacancies was examined. It is common when analysing a surface using experimental techniques that vacancies are detected. For this study an oxygen vacancy on the bridging site was introduced.

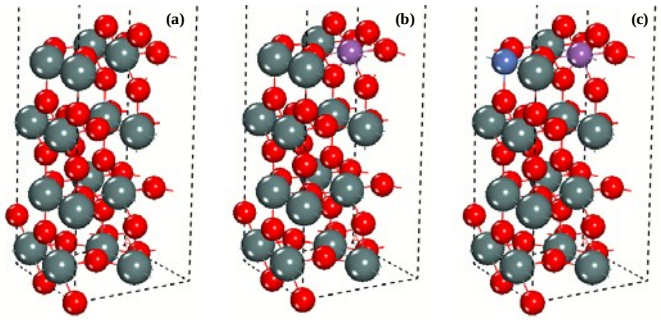

Figure 1 (a) shows the SnO_2 (110) facet, (b) shows the preferred site for Sb doping and (c) shows the preferred doping site for Ni. The grey atoms represent Sn, the purple represent Sb and the blue represent Ni. The black dashed line is the vacuum slab (15 Å).

Surface Adsorption Calculations

The adsorption energy (E_{ads}) of the system was calculated using equation 1:

$$E_{ads} = E_{adsorbate\ on\ surface} - E_{surface} - E_{gas} \qquad (1)$$

where $E_{adsorbate\ on\ surface}$ is the energy of the adsorbate on the surface, $E_{surface}$ is the energy of the surface and E_{gas} is the energy of the corresponding adsorbing species in the gas phase. Equation 1 shows the more negative the adsorption energy is, the greater the adsorption to the surface. Each term in equation 1 must correspond to the same surface coverage, whether this is a pure metal or metal oxide.

Results and Discussion

Most Stable Surface Facet of SnO_2

In agreement with the study reported by Batzill *et al.*[24], the (110) facet was calculated to be most stable and thus the doping with Sb and Ni was carried out on this facet (Figure 2a). It should be noted that although Ni^{2+} is not stable under acidic conditions at the surface, this is reflected by the poor lifetimes for these anodes. Possible solutions to the problem of Ni^{2+} instability is an on-going topic that we are currently studying through the addition of other dopants such as gold, and the results will be published in future papers. Batzill *et al.* also discussed the possibility of surface vacancies or defects, where it was suggested that the SnO_2 was especially susceptible to the presence of an oxygen vacancy (Figure 2b). By creating this vacancy, two cationic Sn sites form which act as Lewis acidic sites and consequently this site tends to be particularly reactive.

Figure 2a shows the most stable arrangement of Ni/Sb-SnO_2, with Sb occupying the bridged region and Ni occupying the top site region. The oxygen vacancy was modelled at different oxygen sites (Figure S1) and it was found that the preferred vacancy was the bridged oxygen close to the Sb as shown in Figure 2b. The results for the other sites tested are shown in the supplementary information (Tables S1-S3).

Journal Name ARTICLE

DOI: 10.1039/C6CP06906A

Surface Oxidants

Upon constructing a stable surface model, the degree of surface oxidation must be determined. As the mechanism being investigated involves the splitting of H_2O, surface oxidants from H_2O adsorption and activation can be calculated and a phase diagram constructed (Figure 3). In this model the Ni/Sb-SnO_2 has four possible active sites on the surface, two on the top-site and two on the bridging site (Figure S2). For this reason it is, therefore, possible to have a surface coverage of 0.25, 0.50, 0.75 and 1.00 ML.

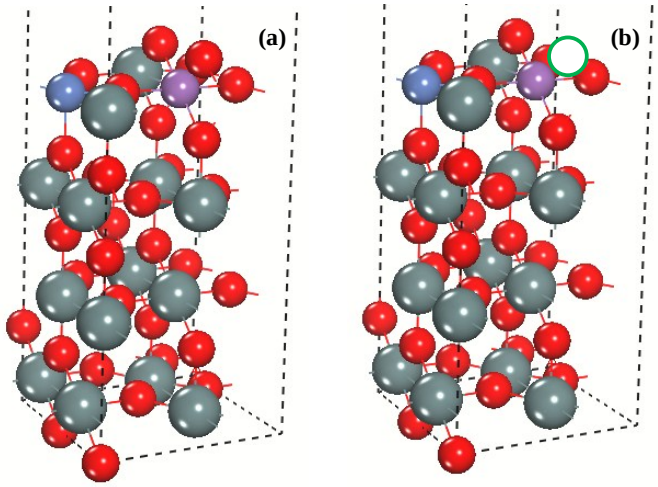

Figure 2 (a) shows the SnO_2 (110) facet doped with Ni and Sb and (b) shows the same surface with an oxygen vacancy. The grey atoms are Sn, the purple is Sb, the blue is Ni and the green circle represents the vacant site.

The main surface oxidants expected are either OH, O or both. The reaction is an oxidation reaction and so corresponds to the loss of electrons and the release of a proton (steps 1 and 2). This proton is capable of surface adsorption (or site hopping) and so is also taken into account.

Construction of Phase Diagrams

In order to construct a phase diagram the energy of each coverage must be calculated. Each calculation will yield an energy value, the free energy of reaction (ΔG_{rxn}). This free energy change can be calculated using equation 2:

$$\Delta G_{rxn} = \Delta E + ZPE - T\Delta S \quad (2)$$

where ΔE is the total energy of the system, ZPE is the zero-point energy, and TΔS is the entropy of the system which also includes the temperature. The free energy change of the system accounts for the zero-point energy and the associated entropy. Temperature is also factored into the free energy, along with the pH correction factor. As this experiment is carried out in an acidic electrolyte (0.5 M H_2SO_4), a pH correction factor (59.13 meV) is used which can be calculated using the following equation:

$$\Delta G(pH) = k_B T \ ln10(pH) \quad (3)$$

where pH is taken as 1, T as 298 K, and Boltzmann's constant k_B is 1.38 x 10^{-23} m^2 kg s^{-2} K^{-1}.

After considering this, the standard free energy (ΔG^0_{rxn}) for the formation of each species is the free energy change at 0 V vs SHE. It is the potential independent contribution to the free energy change for each reaction, therefore, U = 0 V. This comes from $\Delta G_{rxn} = \Delta G^0_{rxn}$, where U is the applied potential.

This is in essence the second part of constructing a phase diagram; determining the value of U at which ΔG_{rxn} is equal to zero, so the potential at which a reaction becomes thermodynamically favourable. To calculate U the following equation must be used:

$$\Delta G_{rxn} = \Delta G^0_{rxn} - eU \quad (4)$$

The e represents the charge of an electron (e= -1) giving the equation below:

$$\Delta G_{rxn} = \Delta G^0_{rxn} + U \quad (5)$$

In a phase diagram, a straight line is given for each oxidant at that specific coverage. This equation is in the form of y = mx + c where the gradient is 1. This form of the equations can be attributed to H formation, so if ΔG_{rxn} is set to zero then U = $-G^0_{rxn}$.

For OH formation, the gradient should be -1, so U = ΔG^0_{rxn}, and for O formation, U = 1/2ΔG^0_{rxn} since two electrons are transferred.

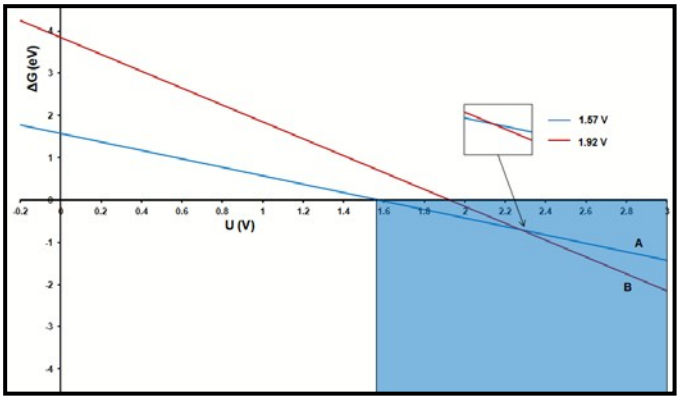

Figure 3 Phase diagram of ΔG of formation of surface oxidants against applied potential (vs. SHE) on the Ni/Sb-SnO_2 surface. The blue line (line A) represents the stability of adsorbed OH with potential and the red line (line B) represents the stability of adsorbed O with potential. The white area represents the potential region in where no surface oxidants are present and the blue area represents the potential region in which OH is the predominant surface oxidant.

Figure 3 shows the phase diagram constructed for OH and O present on the Ni/Sb-SO_2 anode. To interpret a phase diagram, both the lines representing OH and O are observed with the line that intersects the x-axis first considered the dominant surface oxidant. It can be clearly seen that the blue line (OH) intersects the x-axis at a lower potential than the red line (O).

View Article Online
DOI: 10.1039/C6CP06906A

At this crossing point (1.57 V), OH oxidation is dominant, and this is the case at anything above this potential.

Surface H^+ was also tested, but not included in the phase diagram as it was found to occur at a potential of -9.52 V, much lower than the experimental potential of *2.7* V. Considering this, it should be noted that although not included in the phase diagram, surface H^+ does on occasion occur, with H^+ hopping across surface sites between O atoms.

Mechanistic studies of O_3 formation on Ni/Sb-SnO_2

Based on previous results[23], the same method was applied to the Ni/Sb-SnO_2 catalyst to determine the correct mechanism for O_3 formation through the splitting of H_2O, and how the thermodynamics and kinetics are affected as a result. The mechanism investigated has four steps involving including the splitting of H_2O to form O_2 and ultimately O_3 through the interaction of O_2 and surface O as illustrated in reactions 4-7:

$$H_2O \rightarrow OH + H^+ + e^- \quad \text{(R4)}$$
$$OH \rightarrow O + H^+ + e^- \quad \text{(R5)}$$
$$2O \rightarrow O_{2(ads)} \rightarrow O_2 \quad \text{(R6)}$$
$$O_2 + O \rightarrow O_{3(ads)} \rightarrow O_3 \quad \text{(R7)}$$

Steps 1 and 2 (reactions 4 + 5) involve the deprotonation to OH and O and should occur with ease after a potential is applied across the surface of the anode[35]. For this reason the main focus of this study is reactions 6 and 7. Step 3 is the formation of O_2 (Figure 4) and step 4 is the formation of O_3 (Figure 5) from the O_2 formed in step 3 interacting with further surface O.

Step 3 – The formation of O_2

In step 3 two surface O atoms interact with each other to form O_2 (ads). The most stable site for this interaction was across a surface vacancy. This is better seen in reaction 8:

$$2O \rightarrow O_{2(ads)} \rightarrow O_2 \quad \text{(R8)}$$

Reaction 8 shows that the two surface O atoms interact to form O_2 (ads), before desorbing to the gaseous phase. In order to continue to step 4, O_2 must remain adsorbed on the surface for long enough so that the formation of O_3 can occur. The degree to which the O_2 remains adsorbed will help in determining the overall current efficiency (CE). The longer the O_2 is adsorbed the greater the chance for interaction with surface O.

Initial state of reaction (IS)

From the phase diagram (Figure 3) the optimal coverage was determined to be 0.5 ML OH. The IS, two O (ads) atoms that have been formed by the deprotonation of OH. The optimized distance between these two O atoms was 3.38 Å. It is also of note to mention that one of the O atoms is adsorbed on the site with oxygen vacancy (more reactive site)[24].

Transition State of Reaction (TS)

In going from the IS to TS, an activation barrier (E_{act}) must be overcome. The lower the barrier, the easier the reaction will progress. The difference in energy between the TS and IS, i.e. the activation energy was calculated as 0.34 eV.

$$E_{act}(O_2) = E_{TS} - E_{IS} = 0.34\ eV \quad (6)$$

The E_{act} was calculated as 0.34 eV (Figure 4). Thermodynamically this progression should occur with ease. Coupled with the high experimental potential (2.7 V)[36], this results further suggests that the reaction will occur easily as the high potential will drive the reaction in the forward direction to completion forming O_2.

Final State of Reaction (FS)

The FS of the reaction is the formation of O_2. When both top site and bridging O are in close enough proximity to one another they will interact and O_2(ads) is formed. Experimentally, O_3 formation on Ni/Sb-SnO_2 shows a high CE suggesting a large proportion of the O_2 formed stays adsorbed to the surface, with a small proportion being desorbed. In order to determine the stability of O_2, the enthalpy of reaction (ΔG_{rxn}) between the IS and FS is calculated in equation 7:

$$\Delta G_{rxn} = E_{FS} - E_{IS} = -0.47\ eV \quad (7)$$

The ΔG was calculated to be -0.47 eV. The FS is more stable than the IS and minimal O_2 decomposition should occur as a result.

As well as the ΔG_{rxn}, the E_{ads} (O_2) was calculated to determine the stability of O_2 to the surface:

$$E_{ads}(O_2) = E(surface\ O_2) - E(clean\ surface) - E(O_2) = -0.05\ eV \quad (8)$$

The $E_{ads}(O_2)$ was found to be -0.05 eV, with entropy considerations taken into account at 298 K. This adsorption is weak at -0.05 eV but should be noted that the reaction is run as gas phase whereas experimentally an aqueous electrolyte is employed; hence a H_2O stabilization effect[37] will occur, resulting in a more stable adsorption for O_2.

Step 4 – The formation of O_3

Step 4, the formation of O_3, occurs by interaction of surface O_2 formed from step 3 with further surface O obtained through the adsorption of OH:

$$O_2 + O^{\bullet} \rightarrow O_3 \quad \text{(R9)}$$

The adsorption of OH and subsequent deprotonation to O

Experimentally, this reaction is carried out in aqueous electrolyte (0.5M H_2SO_4) with a large concentration of OH passing over the surface from the splitting of H_2O seen in reaction 4. As a result the adsorption of OH is calculated first.

After the most stable arrangement has been determined, this OH is deprotonated creating $O^{\bullet}$ (ads) needed for step 4.
In this deprotonation the Gibbs free energy (ΔG_{rxn}) can be calculated using equation 9:

$$\Delta G_{rxn} = G(O) + G(H^+ + e^-) - G(OH) = 1.96\ eV \qquad (9)$$

Equation 9 shows the Gibbs free energy calculated for the deprotonation of OH being 1.96 eV. This suggests that a minimum potential of 1.96 V is required for the second deprotonation to take place. This is higher than the experimental onset potential, but within the electrochemical window of study, with a potential of 2.7 V applied for Ni/Sb-SnO_2[36].

The reaction of O_2 and O to form O_3

As found for step 3, step 4 will have an IS, TS and a FS. The IS in this step is O_2 (ads) and O (ads). The TS is O_2 (ads) and O (ads), but this time they are in closer proximity to one another. The FS is the formation of O_3 (ads).

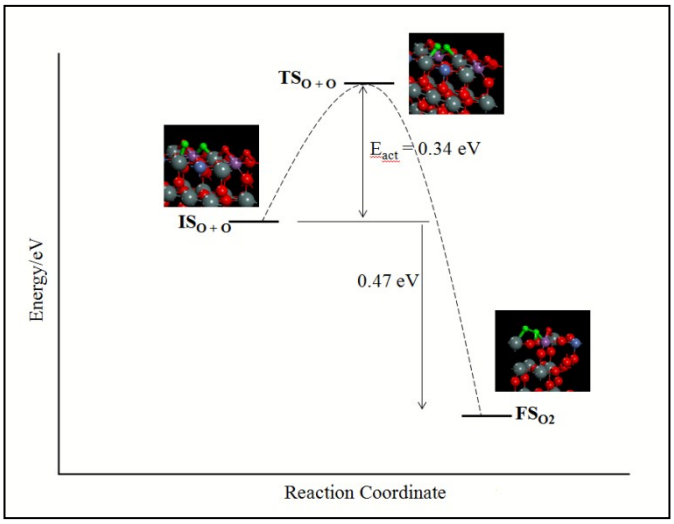

Figure 4 Energy profile for step 3 of the mechanism, the formation of surface O_2 from two adsorbed O atoms. The atoms highlighted in green are the interacting atoms in the mechanism. The initial state shows the adsorbed O and bridging surface O, the transition state shows both these atoms in a closer proximity to one another, and the final state shows both atoms bonded to form surface O_2.

Initial State of Reaction (IS)

The IS of the reaction is O_2 (ads) and O (ads). The optimised bond distance between these two is 3.35 Å with the O (ads) adjacent to the O_2 (ads) from step 3.

Transition State of Reaction (TS)

The TS is the point which is highest in energy. The bond distance is greatly reduced from 3.35 Å to 1.75 Å. After running a subsequent frequency calculation, one of the frequency values is imaginary (f/i) and so the TS is deemed suitable.
E_{act} was calculated from equation (10):

$$E_{act}(O_3) = E_{TS} - E_{IS} = 0.77\ eV \qquad (10)$$

The E_{act} associated with this step was found to be 0.77 eV. Although there is not a maximum value for the E_{act}, the higher the barrier the slower the reaction. However, the rate of reaction with a lower E_{act} (less than 0.77 eV) would be expected to proceed at a faster rate. These calculations have been performed in the gas phase, whereas experimentally the reaction occurs in liquid phase (electrolyte solution). If this step had been run in the presence of H_2O across the surface, the barrier would be expected to be lower due to the water stabilisation effect[37]. The potential for this reaction is 2.7 V. This is quite a high potential and will aid in driving the reaction to completion and should occur with ease.

Final State of Reaction (FS)

The FS of the reaction is the formation of surface O_3 (ads). When surface O_2 and $O^{\bullet}$ from the IS are close enough in proximity (less than 1.75 Å), they interact with each other to form surface O_3 (ads). To determine the stability of O_3 (ads), both the E_{ads} and ΔG_{rxn} are taken into account:

$$\Delta G_{rxn} = E_{FS} - E_{IS} = -0.05\ eV \qquad (11)$$

The ΔG change is small at -0.05 eV, suggesting a slightly more favourable FS (Figure 5). This agrees with what the thermodynamics suggest, that O_2 is thermodynamically more stable than O_3, and so the O_3 will readily decompose back to O_2 and O via the reverse process. This is why a high overpotential is required for O_2 formation. Through this high overpotential, the O_2 sites would be inhibited and thus promote O_3 formation, hence stopping this decomposition
As well as the ΔG, the E_{ads} (O_3) can be calculated to determine the stability of O_3 on the surface:

$$E_{ads}(O_3) = E(surface\ O_3) - E(clean\ surf.) - E(O_3) = -0.15\ eV \qquad (12)$$

An E_{ads} (O_3) of -0.15 eV shows the adsorption energy taking into account entropy, highlighting the stability of O_3 at 298 K.
Figure 5 shows the reaction pathway for the formation of O_3 through the interaction of surface O_2 and O. The reaction is found to occur via a Langmuir-Hinshelwood mechanism where two species adsorb to the surface (O_2 and O), the diffuse across the surface interacting with each other before desorbing as a molecule (O_3). This is interesting as the same mechanism run on β-PbO_2 previously [23], showed that the formation of O_3 preferred to occur via an Eley-Rideal mechanism where the O_2 passes over the surface and interact with an adsorbed species forming O_3 and desorbing. This shows that although the formation of O_3 occurs via the same reaction step, the chemistry of each catalyst is not necessarily the same, and thus this could have an overall effect of the CE of O_3 as a result. For β-PbO_2 the E_{ads} (O_3) was -0.50 eV and for Ni/Sb-SnO_2 it was -0.15 eV with entropy considerations. Although the adsorption is stronger on the β-PbO_2 surface the

CE values are much higher for Ni/Sb-SnO_2; this is because the adsorption energy is too strong hence the active sites become blocked easier resulting in a lower CE.

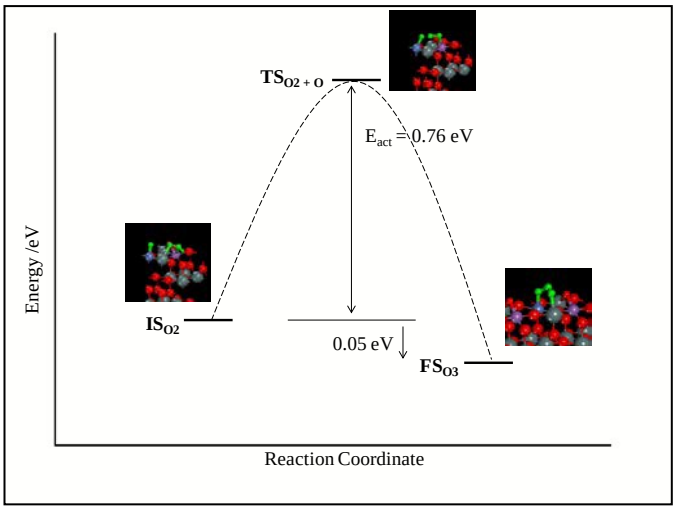

Figure 5 Energy profile for step 4 of the mechanism, the transformation from O_2 and O to O_3. The atoms highlighted in green are the interacting atoms in the mechanism. The initial state shows the O_2 (ads) and O (ads), the transition state shows both these atoms in a closer proximity to one another, and the final state shows both atoms bonded to form surface O_3.

Catalyst Regeneration

When choosing a catalyst, it is not only activity and selectivity that are important, but also the lifetime. For a catalyst with a long lifetime, it must be able to regenerate itself. This is an area that needs improve upon with regards to the EOP mechanism and the Ni/Sb-SnO_2 anodes are said to have a moderate lifetime. Examining equation 12, which shows the E_{ads} (O_3), it can be seen that the calculated value of adsorption for O_3 was -0.15 eV. In order to make a catalyst regenerable this O_3 must be easily displaced in order to increase the lifetime, thus making the anode regenerable, freeing up the active sites for EOP. When trying to desorb the O_3 using DFT it was found the O_3 preferred to re-adsorb onto the surface, hence enhancing its stability. This DFT study does not account for some experimental factors such as potential and flow rate. It is also the case that this study involves the gas phase reaction, whereas experimentally an aqueous acidic electrolyte is employed. One final thing to consider is that this study shows the successful formation of a single O_3 molecule on the Ni/Sb-SnO_2, whereas when run experimentally there may be multiple O_2 and O_3 molecules along with other OH and O intermediates on the surface at the one time. As a result there will be electrostatic repulsion between the competing adsorbates thus weakening the adsorption leading to the successful desorption of O_3. Taking all of this into account and the literature with regards to high CE values quoted, the catalyst can clearly represent one that is regenerable and future work needs to be done both experimentally and theoretically to discover new methods of increasing the overall lifetime.

Conclusions

View Article Online
DOI: 10.1039/C6CP06906A

The H_2O splitting mechanism is one well studied experimentally on Ni/Sb-SnO_2 for O_3 formation. The study of the mechanism using DFT is a first attempt from a theoretical perspective. Using DFT calculations, possible pathways including E_{act} and E_{ads} were determined and a suitable reaction mechanism with the formation of O_3 occurring via a Langmuir Hinshelwood surface reaction was identified. By calculating SnO_2 (110) as the most stable facet, further studies into the doping of the top layer (surface) with Sb and Ni were performed with a model catalyst generated. The concept of surface vacancies (oxygen vacancies) was introduced into the model catalyst and the electrochemical ozone production (EOP) mechanism run. Future studies on this system need to be carried out to first model the EOP mechanism with O_3H as the intermediate, offering a comparison to the direct O_3 formation discussed within this paper. The effect of the oxygen vacancy on the E_{act} and E_{ads} needs to be further investigated with comparisons between the reaction energy of a system with an oxygen vacancy and opposed to one without an oxygen vacancy.

Acknowledgements

We thank the Department of Education and Learning (DEL) of Northern Ireland for funding this project, and Loughborough University and the University of Manchester for their support.

Notes and references

1. L. G. C. Villegas, N. Mashhadi, M. Chen, D. Mukherjee, K. E. Taylor and N. Biswas, *Cur. Poll. Rep.*, 2016, **2**, 157.
2. H. Suzuki, S. Araki and H. Yamamoto, *J. Wat. Proc. Eng.*, 2015, **7**, 54.
3. L. Kovalova, H. Siegrist, U. von Gunten, J. Eugster, M. Hagenbuch, A. Wittmer, R. Moser and C. S. McArdell, *Environ. Sci. Tech.*, 2013, **47**, 7899.
4. J. Luyten, K. Sniegowski, K. Van Eyck, D. Maertens, S. Timmermans, S. Liers and L. Braeken, *Wat. Sci. Tech.*, 2013, **68**, 2048.
5. A. Chin and P. R. Bérubé, *Wat. Res.*, 2005, **39**, 2136.
6. D. Iliadis and B. J. Millar, *Open. J. Stom.*, 2013, **3**, 197.
7. L. Franken. *White Paper*, 2005.
8. C. S. Sousa, L. M. Torres, M. P. F. Azevedo, T. C. d. Camargo, K. U. Graziano, R. A. Lacerda and R. N. T. Turrini, *Rev. Esc. Enferm. USP.*, 2011, **45**, 1243.
9. T. Iwamura, K. Nagano, T. Nogami, N. Matsuki, N. Kosaka, H. Shintani and M. Katoh, *Biocontrol. Sci.*, 2013, **18**, 9.
10. A. N. Onyango, *J. Chem. Biol.*, 2016, **9**, 1.
11. L. M. d. Silva, M. H. P. Santana and J. F. C. Boodts, *Química Nova,* 2003, **26**, 880.
12. R.D. Letterman, Water Quality and Treatment - A Handbook of Community Water Supplies. *5th Ed*.
13. A. A. Babak, R. Amadelli and V. N. Fateev, *Russ. J. Electrochem.*, 1998, **34**, 149.
14. M. I. Awad, S. Sata, K. Kaneda, M. Ikematsu, T. Okajima and T. Ohsaka, *Electrochem. Comm.*, 2006, **8**, 1263.

View Article Online
DOI: 10.1039/C6CP06906A

15. P. C. Foller and C. W. Tobias, *J. Electrochem. Soc.*, 1982, **129**, 506.
16. J. Wang, X. Li, L. Guo and X. Luo, *App. Surf. Sci.*, **2008**, 254, 6666.
17. J. Wang and X. Jing, *J. Electrochem.*, 2006, **74**, 539.
18. M. A. García-Morales, G. Roa-Morales, C. Barrera-Díaz, B. Bilyeu and M. A. Rodrigo, *Electrochem. Comm.*, 2013, **27**, 34.
19. K. Arihara, C. Terashima and A. Fujishima, *J. Electrochem. Soc.*, 2007, **154**, E71.
20. J. Basiriparsa and M. Abbasi, *J. Solid. State. Electrochem.*, 2012, **16**, 1011.
21. P. A. Christensen and A. Imkum, *Ozone Sci. Eng.*, 2011, **33**, 389.
22. Y. Wang, H., S. Cheng, K.-Y. Chan and X. Y. Li, *J. Electrochem.*. Soc., 2005, **152**, D197.
23. G. Gibson, A. Morgan, P. Hu and W.-F. Lin, *Chem. Phys. Lett.*, 2016, **654**, 46.
24. M. Batzill and U. Diebold, *Prog. Surf. Sci.*, 2005, **79**, 47.
25. G. Kresse and J. Furthmüller, *Phys. Rev. B*, 1996, **54**, 11169.
26. G. Kresse and J. Furthmüller, *Comput. Mat. Sci.*, 1996, **6**, 15.
27. G. Kresse and J. Hafner, *Phys. Rev. B.*, 1994, **49**, 14251.
28. J. P. Perdew, K. Burke and M. Ernzerhof, *Phys. Rev. Lett.*, 1996, **77**, 3865.
29. G. Kresse and D. Joubert, *Phys. Rev. B.*, 1999, **59**, 1758.
30. P. E. Blöchl, *Phys. Rev. B.*, 1994, **50**, 17953.
31. A. Michaelides, Z. P. Liu, C. J. Zhang, A. Alavia, D. A. King, P. Hu, *J. Am. Chem. Soc.*, 2003, **125**, 3704.
32. Z.-P. Liu and P. Hu, *J. Am. Chem. Soc.*, 2003, **125**, 1958.
33. A. Alavia, P. Hu, T. Deutsch, P. L. Sylvestrelli and J. Hutter, *J. Phys. Rev. Lett.*, 1998, **80**, 3650.
34. H. J. Monkhorst and J. D. Pack, *Phys. Rev. B.*, 1976, **13**, 5188.
35. J. Liu, X.-M. Cao and P. Hu, *Physical Chemistry Chemical Physics*, 2014, **16**, 4176-4185.
36. P. A. Christensen, W. F. Lin, H. Christensen, A. Imkum, J. M. Jin, G. Li and C. M. Dyson, *Ozone. Sci. Eng.*, 2009, **31**, 287.
37. R. Kavanagh, X.-M. Cao, W.-F. Lin, C. Hardacre and P. Hu, *Angew. Chem. Int. Ed.*, 2012, **51**, 1572.